

Stability-superconductivity map for compressed Na-intercalated graphite

Shashi B. Mishra, Edan T. Marcial, Suryakanti Debata, Aleksey N. Kolmogorov, and Elena R. Margine
Department of Physics, and Astronomy, Binghamton University-SUNY, Binghamton, New York 13902, USA

(Dated: July 24, 2024)

A recent *ab initio* investigation of Na-C binary compounds under moderate pressures has uncovered a possible stable NaC₄ superconductor with an estimated critical temperature up to 41 K. We revisit this promising binary system by performing a more focused exploration of Na-intercalated graphite configurations, assessing the sensitivity of their thermodynamic stability to density functional approximations at different (T, P) conditions, and examining their superconducting properties with the anisotropic Migdal-Eliashberg formalism. The combinatorial screening of possible Na arrangements reveals additional stable stoichiometries, *i.e.*, Na₃C₁₀, NaC₈, NaC₁₀, and NaC₁₂, that redefine the previously proposed convex hulls for pressures up to 10 GPa. The evaluation of formation enthalpies with different van der Waals functionals indicates that the proposed compounds might not be thermodynamically stable at zero temperature but some of them could stabilize due to the vibrational entropy or form via cold compression if graphite is used as a starting material. Our more rigorous modeling of the electron-phonon coupling in NaC₄ confirms the material's potential for high-temperature superconductivity, with a critical temperature reaching 48 K at 10 GPa, and reveals a well-defined two-gap structure unusual for an electron-doped compound. By tracking the position of the intercalant nearly free electron states with respect to the Fermi level in viable Na-C compounds, we map out the range of pressures and compositions needed for strong electron-phonon coupling and identify Na₃C₁₀ as an equally promising superconductor.

I. INTRODUCTION

Carbon-based materials offer a rich playground in the quest for thermodynamically stable superconductors at ambient and low pressure [1–7]. Graphite intercalation compounds (GICs) [8], in particular, have been known to superconduct since the mid 1960s when superconductivity below 1 K was discovered in graphite intercalated with alkali metals (AC₈ with A = K, Rb, and Cs) [9]. Since then, considerable efforts have been made to find superconductivity in GICs at elevated temperatures, and the search has been focused on increasing the charge transfer from the intercalant atoms to the host graphene sheets by varying the stoichiometry and the intercalant type. To date, YbC₆ and CaC₆ with critical temperature (T_c) values of 6.5 and 11.5 K stand as the highest temperature superconductors in this class under ambient conditions [10, 11]. Superconductivity has also been induced or enhanced by applying external pressure. For instance, LiC₂ and NaC₂ become superconductors with $T_c = 1.9$ K at 3.3 GPa [12] and $T_c = 5.0$ K at 3.5 GPa [13], while in CaC₆ a maximum value of 15.1 K is reached at 7.5 GPa [14].

Recently, an *ab initio* evolutionary structure search in the Na-C system has identified a new GIC at the 1:4 composition [15]. The NaC₄ phase with the oS20 Pearson symbol and $Cmcm$ symmetry (Fig. 1(c)) was predicted to stabilize above 8.9 GPa and have a maximum T_c of 41.2 K at 5 GPa. While this work has shown that the electron-phonon (e-ph) coupling is strong enough to yield a T_c above the record 39 K value in MgB₂ based on the Allen-Dynes modified McMillan formula [16, 17], the nature of the superconducting gap has not been investigated.

Our present study reexamines the stability and superconductivity of Na-C candidate materials under pressures

up to 10 GPa. Further exploration of the vast configuration space was motivated by the well-known difficulty of locating thermodynamically stable compounds even with the most advanced structure optimization methods [18–21]. For instance, our unconstrained evolutionary searches yielded a number of new complex crystal structures that have either been confirmed experimentally [22–24] or inspired the creation of more stable derivatives based on the identified favorable motifs [25–29]. In the latest investigation of layered metal borocarbides, we generated viable quaternary phases via systematic screening of possible metal decorations within ideal or modified honeycomb frameworks [28]. Application of this strategy to Na-C in the present work resulted in a significant revision of the previously proposed ground states. The updated set at 10 GPa contains large-sized oP104-Na₃C₁₀, oP18-NaC₈, oS44-NaC₁₀, and hP13-NaC₁₂ phases that make mP12-NaC₂ metastable and oS20-NaC₄ marginally stable.

Importantly, we demonstrate that the global stability of these van der Waals solids is very sensitive to the treatment of the dispersive interactions. While the Na-C are thermodynamically stable in the optB88-vdW approximation of the non-local density functional [30], as was shown in Ref. [15], they have positive formation enthalpies in our optB86b-vdW [31] calculations. Fortunately, the inclusion of vibrational entropy brings them closer to stability and makes Na₃C₁₀ a true ground state at room temperature. Moreover, we argue that the feasibility of obtaining the binary layered intercalated compounds should be evaluated with respect to graphite rather than diamond, provided that the synthesis starts with the former material and the (T, P) conditions are kept sufficiently low to avoid the sp^2 to sp^3 transformation. When referenced to the layered carbon poly-

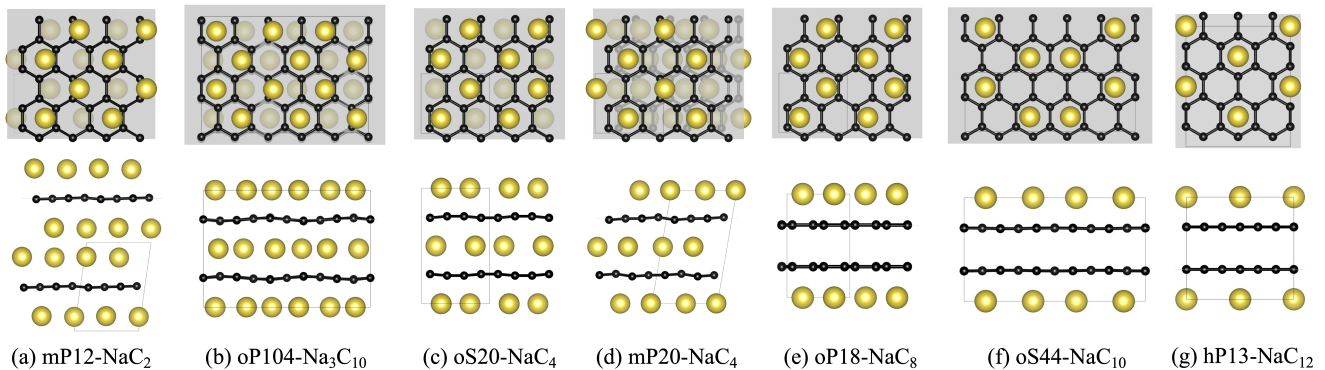


FIG. 1. Select high-pressure Na-C phases found to be viable in previous [15] (a,c) and present (b,d,e,f,g) *ab initio* studies. The top and side views show the corresponding distributions of Na (large yellow spheres) intercalated between C honeycomb layers (small black spheres).

morph, the Na-intercalated variants have negative formation Gibbs free energies.

Finally, we probe the proposed materials for superconducting properties. We analyze the position of the intercalant nearly free electron states across different phases and pressures to establish conditions needed for strong e-ph coupling. According to the constructed composition-pressure map, Na_3C_{10} compound with a complex structure has promise to be a high- T_c superconductor. We further study oS20- NaC_4 at 10 GPa using the fully anisotropic Migdal-Eliashberg (aME) formalism [32–34]. The aME method has been demonstrated to yield significantly higher estimates of the critical temperature, by a factor of two to three, in related layered conventional superconductors, *i.e.*, metal borides and borocarbides [32, 35–40]. We calculate the momentum dependence of the e-ph coupling and superconducting energy gap on the Fermi surface. Our aME calculations yield a T_c of 48 K, which is slightly larger than the estimate of 39 K obtained in the previous work using an isotropic treatment of the e-ph coupling [15].

II. METHODS

We examined the stability of the Na-C phases with VASP [41] using projector augmented wave potentials [42]. By default, the non-local van der Waals interactions were treated with the optB86b-vdW functional [31], but also checked with alternative optB88-vdW [30] and r²SCAN+rVV10 [43, 44] functionals. Dense Monkhorst-Pack k -point meshes with $\Delta k \sim 2\pi \times 0.025 \text{ \AA}^{-1}$ and a plane-wave cutoff of 500 eV ensured numerical convergence to typically within 1 meV/atom. To systematically screen possible decorations of interlayer sites, we constructed supercells with up to 42 atoms by expanding the stoichiometric MgB_2 prototype and sequentially removing metal atoms. For detection and elimination of equivalent configurations, we relied on our radial distribution function fingerprint [24]. We

calculated thermodynamic corrections due to the vibrational entropy using the finite displacement method implemented in PHONOPY [45], employing supercells sized between 52 and 128 atoms and applying 0.1 Å displacements within the harmonic approximation. Full structural information for select phases is provided in the form of CIF files in Supplemental Material [46].

For calculating properties related to superconductivity, we employed the Quantum ESPRESSO (QE) package [47] with the optB86b-vdW functional [31, 48, 49] and optimized norm-conserving Vanderbilt pseudopotentials (ONCVSP) [50] from the Pseudo Dojo library [51] generated with the relativistic Perdew-Burke-Ernzerhof parametrization [52]. We used a plane-wave cutoff of 100 Ry, a Methfessel-Paxton smearing [53] value of 0.02 Ry, and Γ -centered \mathbf{k} -grids of $12 \times 12 \times 8$ for oS52- Na_3C_{10} and NaC_{12} , $6 \times 6 \times 4$ for oP104- Na_3C_{10} , $16 \times 16 \times 16$ for NaC_4 and NaC_8 , and $12 \times 12 \times 12$ for NaC_{10} to describe the electronic structure. The lattice parameters and atomic positions were relaxed until the total enthalpy was converged within 10^{-6} Ry and the maximum force on each atom was less than 10^{-4} Ry/Å. The dynamical matrices and the linear variation of the self-consistent potential were calculated within density-functional perturbation theory [54] on \mathbf{q} -meshes of $3 \times 3 \times 2$ for oS52- Na_3C_{10} , $4 \times 4 \times 4$ for NaC_4 and NaC_8 , $3 \times 3 \times 3$ for NaC_{10} , and $4 \times 4 \times 4$ for NaC_{12} .

To investigate e-ph interactions and superconducting properties of NaC_4 further, we used the EPW code [32, 33, 55, 56]. The electronic wavefunctions required for the Wannier interpolation [57, 58] were obtained on a uniform Γ -centered $8 \times 8 \times 8$ \mathbf{k} -grid. We used ten atom-centered orbitals to describe the electronic structure of NaC_4 , with one s orbital for each Na atom and one p_z orbital for each C atom. The anisotropic Migdal-Eliashberg equations were solved on fine uniform $80 \times 80 \times 80$ \mathbf{k} - and $40 \times 40 \times 40$ \mathbf{q} -point grids, with an energy window of ± 0.2 eV around the Fermi level and a Matsubara frequency cutoff of 1.0 eV. When solving the isotropic ME equations, the Dirac deltas of electrons and phonons were

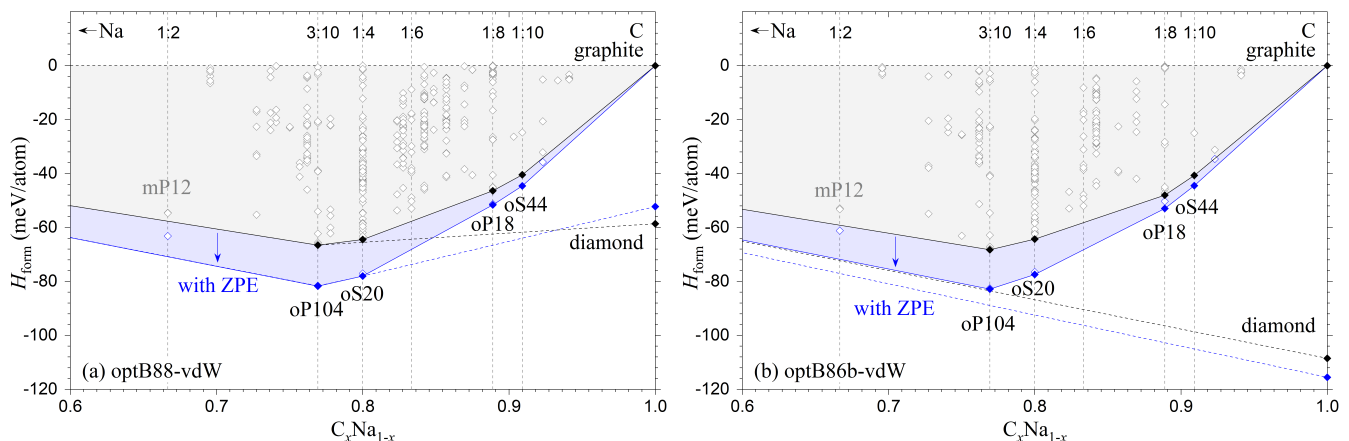


FIG. 2. Stability of Na-C phases at 10 GPa calculated with (a) the optB88-vdW functional or (b) the optB86b-vdW functional. The global (local) convex hulls are denoted with solid (dashed) lines. The formation enthalpies are shown with and without zero-point energy (ZPE) in blue and gray, respectively.

replaced by Gaussians of width 50 meV and 0.3 meV, respectively.

III. RESULTS AND DISCUSSIONS

A. Structure and stability of Na-C compounds

The global evolutionary searches by Hao *et al.* [15] provide an important baseline for viable morphologies in the Na-C binary up to 10 GPa. Namely, only graphite configurations intercalated with either one or two layers of Na appear to compete for thermodynamic stability across the composition range. We reproduce the negative formation enthalpy values evaluated with the optB88-vdW functional for the reported oS20-NaC₄ (−17.3 meV/atom) and mP12-NaC₂ (−15.9 meV/atom) phases relative to bcc-Na and diamond at 10 GPa. At the same time, we observe a high sensitivity of the results to phonon contributions and DFT approximations due to the starkly different bonding types displayed by the binary and reference phases. The inclusion of the zero-point energy (ZPE) alone shifts the values to −36.2 meV/atom and −28.4 meV/atom, respectively, and the vibrational entropy further stabilizes the intercalated compounds (see Fig. 2). The beneficial effect of temperature may be consequential because the formation enthalpies calculated in the optB86b-vdW approximation are positive, at 28.2 and 23.7 meV/atom, and the formation Gibbs free energies turn negative only at about 600 K. Considering the wide range of enthalpy values of graphite relative to diamond, 59, 88, and 116 meV/atom produced by the optB88-vdW, r²SCAN+rVV10, and optB86b-vdW functionals, respectively, it is evident that the systematic errors are too large to make a definitive conclusion about the global stability of the Na-C intercalated phases.

Fortunately, the diamond reference is likely irrelevant if graphite is used as the starting material in the synthesis of the proposed binary compounds and the sample is not heated to high temperatures required to induce the *sp*² to *sp*³ rebonding. The well-established phase diagram for elemental C [59] and the experimental data on the kinetics of the transformation [59] indicate that graphite survives up to 15 – 30 GPa at room temperature. The increase in the interlayer spacing and the transfer of the negative charge to the C layers caused by Na intercalation may affect the kinetic barriers but are not expected to appreciably facilitate the rebonding in the targeted (*T*, *P*) range. Therefore, we find it more appropriate to define the synthesizability of the GICs with respect to bcc-Na and graphite rather than diamond. Figure 2 shows that the two proposed phases are indeed thermodynamically favorable with respect to the C layered polymorph, and the relative enthalpies agree well in the optB86b-vdW and optB88-vdW approximations due to the similarity of the elemental and binary morphologies.

Our screening of larger-sized intercalated structures offers further insight into what phases may form under pressure in this binary system. Starting with 14 different supercells of the MgB₂ or mP12-NaC₂ prototypes, we generated ~ 750 unique Na_{*x*}C₂ configurations and fully optimized them at 10 GPa. The considered phases had hexagonal (7%), orthorhombic (48%), monoclinic (38%), or trigonal (7%) unit cells with up to 52 atoms at 35 compositions below 1:2.

At the 1:4 stoichiometry corresponding to the previously proposed oS20 ground state, we find an alternative mP20 structure that is nearly degenerate in Gibbs free energy with oS20 in both optB86b-vdW and optB88-vdW calculations (see Figs. S1 and S2 in Supplemental Material [46]). The two phases have fairly uniform metal decorations but the monoclinic variant features a pronounced interlayer shift that positions Na atoms near

hexagon centers in one of the two sandwiching C layers (Figs. 1(c) and 1(d)). The structural frustration with respect to shear in these and other examined Na-C phases results in soft phonon modes that are difficult to converge.

The dominant compound at 10 GPa actually occurs at an unusual 3:10 composition in all considered vdW approximations (Figs. 2 and S3 in Supplemental Material [46]). The best oS52 structure with the $Cmcm$ symmetry in the generated pool had multiple imaginary modes across the Brillouin zone. The displacement of the atoms along the only imaginary mode at Γ point corresponding to an interlayer shift lowered the symmetry to oS52 ($C222_1$) and the energy by 0.7 meV/atom but did not make the structure dynamically stable (see Fig. S4 [46]). We doubled the shortest lattice constant (a) and repeated the procedure, further lowering the symmetry to oP104 ($P2_12_12_1$) and energy by 0.5 meV/atom. Unfortunately, the phonon dispersion still displays branches with imaginary frequencies (see Fig. S5 [46]) and additional distortions leading to, *i.e.*, mP104 ($P2_1$), produce negligible gains in energy. The situation is not uncommon and cannot always be resolved [25, 60, 61]. We consider the oP104 structure an adequate model for the frustrated compound and use it in the thermodynamic stability analysis (the presence of slightly imaginary modes has an insignificant effect on the vibrational entropy). Figure 1(b) shows that, just as in oS20-NaC₄, the Na atoms are not in perfect registry with the honeycomb lattice but a third of them do reside above and below the C hexagon centers.

The oP104-Na₃C₁₀ destabilizes the proposed double-layer mP12-NaC₂ phase at 10 GPa but leaves room for possible GICs at the low-Na composition end, such as NaC₈ and NaC₁₀. Figures 1(e) and 1(f) illustrate that the most favored configurations feature nearly flat C layers and Na intercalating every other gallery, known as stage-two GICs. The lower Na concentration allows the metal sublattice to find a better balance between even distribution and registry with the honeycomb lattice. Consequently, oS44-NaC₁₀ and oP18-NaC₈ are found to be dynamically stable (see Fig. S4 [46]).

The resulting local convex hull (relative to graphite) at 0 K and 10 GPa is defined by the four phases at the 3:10, 1:4, 1:8, and 1:10 compositions in all optB86b-vdW, optB88-vdW, and r²SCAN+rVV10 approximations (Figs. 2 and S3 [46]). The set remains unchanged at elevated temperatures once the vibrational entropy is included (Figs. S1 and S2 in Supplemental Material [46]). Interestingly, oP104-Na₃C₁₀ is the only intercalated phase that is globally stable at room temperature in both DFT treatments (Fig. 2). To probe what GICs could be stable in the 1 – 10 GPa range, we reoptimized relevant phases at select pressures and constructed corresponding local convex hulls at 0 K (Fig. 3). The first material to stabilize under compression is actually a stage-two hP13-NaC₁₂ GIC derived from the $\sqrt{3} \times \sqrt{3} \times 2$ supercell of MgB₂. mP12-NaC₂ may indeed form just

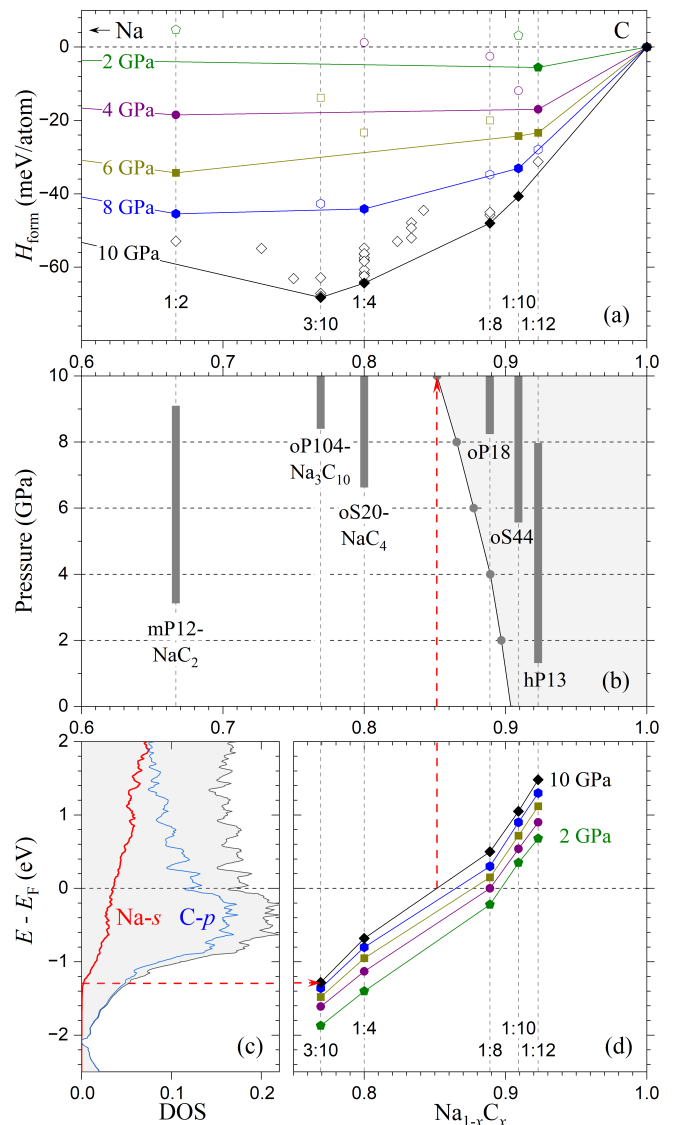


FIG. 3. Stability and electronic properties of $\text{Na}_{1-x}\text{C}_x$ compounds calculated with the optB86b-vdW functional. (a) Convex hulls with respect to bcc Na and graphite at 2–10 GPa. (b) Stability ranges of the stable Na-C phases. The shaded area marks the (x, P) phase space in which Na-C materials are not expected to have electron-doped Na-*s* states important for superconductivity. (c) Density of states in oP104-Na₃C₁₀. The dashed red line showing the bottom of the Na-*s* states. (d) Position of the Na-*s* band edge for the intercalated Na-C compounds at 2–10 GPa. The dashed red line marks an approximate composition at which the Na-*s* band edge is expected to align with E_F at 10 GPa.

above 3 GPa (a related LiB compound with double metal layers has been synthesized via cold compression above 23 GPa [62]). The four proposed materials between the 3:10 and 1:10 ratios require higher pressures to be viable (Fig. 3(b)).

B. Electronic and vibrational properties of Na-C phases

To screen the Na-C binary system for possible high- T_c superconductivity, we investigated the electronic and vibrational properties in the proposed set of intercalated phases, oS52 (oP104)- Na_3C_{10} , oS20 (mP20)- NaC_4 , oP18- NaC_8 , oS44- NaC_{10} , and hP13- NaC_{12} , at pressures up to 10 GPa. First, we examined the response of the intercalant Na- s states to composition and pressure to determine conditions under which the band crosses the Fermi level. The presence of the partially occupied nearly free electron states has been linked to superconductivity in several layered compounds (*i.e.*, CaC_6 and YbC_6 GICs [63–65], bilayer C_6CaC_6 [66, 67], monolayer LiC_6 [68, 69], and LiB [38, 70]). The strong interaction of this band with the surrounding lattice has been rationalized as a response to both quantum confinement and electrostatic effects [68, 71, 72].

Our electronic band structure and DOS calculations show that only two of the considered compounds, Na_3C_{10} and NaC_4 , have partially occupied Na- s states in the considered pressure range. Just as in LiB [70], compression from 1 GPa to 10 GPa raises these nearly free electron states by about 1.5 eV. Fortunately, the band edge remains at -1.3 eV and -0.7 eV below the Fermi level in the two respective Na-C compounds at 10 GPa (Figs. 3(c) and 4). The data in Figs. 3(b) and 3(d) and Fig. S4 in Supplemental Material [46] illustrate that none of the carbides with the lower metal content feature the Na- s states at the Fermi level in the corresponding regions of thermodynamic stability. For instance, this band would be partially occupied in oP18- NaC_8 below 4 GPa but the phase requires over 8 GPa to break the convex hull. To construct an approximate $x(P)$ boundary between $\text{Na}_{1-x}\text{C}_x$ compounds with and without populated Na- s states, we estimated the critical concentrations x by linear interpolations at every 2 GPa pressure (the dashed red line across panels (b) and (d) of Fig. 3 illustrates the determination of the point at 10 GPa). The near-linear shift of the critical compositions with pressure found for the phases with different symmetries suggests little sensitivity of the Na- s energies to the particular decoration of the metal sites as long as the arrangements within galleries are fairly uniform (see Fig. 1). The resulting shaded area in Fig. 3(b), extrapolated down to the ambient pressure, marks the $x(P)$ region in which Na-C phases are not expected to have superconductivity arising primarily from the strong coupling to the intercalant states.

To check the validity of this observation, we evaluated the e-ph coupling by calculating the Eliashberg spectral function for this set of materials using the QE package and estimated their T_c using the Allen-Dynes equation [17] with $\mu^* = 0.1$. We denote the e-ph coupling strength and the critical temperature obtained with QE as λ^{QE} and T_c^{QE} , respectively, to differentiate them from the EPW values discussed in the next section. Unsurprisingly, the three phases in the gray region probed within

their respective stability regions oP18 at 10 GPa, oS44 at 10 GPa, and hP13 at 5 GPa, were found to have low λ^{QE} of 0.20, 0.18, and 0.18, respectively, with no measurable T_c^{QE} values.

For oS20- NaC_4 at 10 GPa, our calculations produced λ^{QE} and T_c^{QE} values of 1.13 and 33.4 K, comparable to 0.99 and 38.8 K found previously for this material with similar settings except for the use of a different functional [15]. In addition, the competing mP20- NaC_4 structure has lower $\lambda^{\text{QE}} = 0.89$ and $T_c^{\text{QE}} = 28.5$ K. Due to the dynamical instability of the Na_3C_{10} large-sized representative models, we could obtain only crude estimates of the compound's superconducting properties by disregarding all imaginary frequencies in the calculation of $\alpha^2 F(\omega)$ and ω_{log} . The relatively high λ^{QE} (T_c^{QE}) values of 1.39 (37.7 K), and 1.50 (29.6 K) obtained at 10 GPa for the alternative oS52 ($Cmcm$) and oS52 ($C222_1$) structural models indicate that Na_3C_{10} should be as good a superconductor as oS20- NaC_4 . Hence, we believe that the conclusions drawn from our following in-depth analysis of the superconducting properties in NaC_4 should be transferable to the neighboring Na_3C_{10} compound.

C. Superconducting properties of NaC_4

With the oS20- NaC_4 phase determined to stabilize above 6.5 GPa, we perform a more detailed examination of its properties at 10 GPa. A noticeable feature in the electronic structure of NaC_4 in Figs. 4(a) and 4(b) is the presence of a van Hove singularity (vHS) peak near the Fermi level. This gives rise to a sizable DOS at E_F , with $N(E_F) = 0.10$ states/(eV·spin·atom), a value closer to that of 0.11 states/(eV·spin·atom) reported for CaC_6 [74]. The orbital DOS decomposition shows that nearly 85% of $N(E_F)$ comes from the anti-bonding C- π^* states, while the remaining 15% arises predominantly from the Na- s states. As in CaC_6 , there is no notable contribution of the C- σ states to DOS at E_F .

More insight into the electronic structure can be obtained by analyzing the dispersion of NaC_4 with Na atoms removed (empty graphite-like C_4 structure, solid black lines) and the one with C atoms removed (empty Na metal structure, red dashed lines) depicted in Fig. 4(c). Comparing Figs. 4(a) and 4(c), we can interpret the band structure of NaC_4 as a superposition of the C_4 and Na bands. To facilitate this comparison, the C and Na bands in Fig. 4(c) are shifted downward and upward by ~ 2 eV, respectively, to match the Fermi level in NaC_4 . Effectively, the relative shift is equivalent to a charge transfer from the Na atoms to the graphene layers. This can be clearly visualized from the charge density difference plot in Fig. 4(d), where the red and green lobes represent the charge accumulation and depletion regions around the C and Na atoms, respectively. Integrating the atomic-projected DOS, we extract the Löwdin charge for each atom. In NaC_4 , we find a charge transfer of 0.21 electrons/C atom, whereas in CaC_6 each C atom

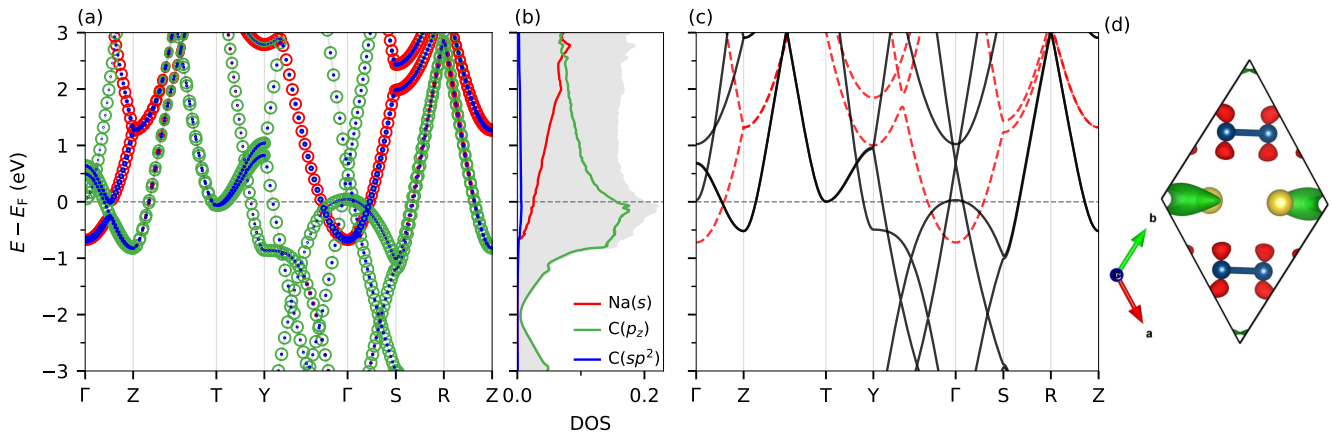


FIG. 4. (a) Electronic band structure and (b) density of states (DOS) in (states/(eV·spin·atom)) of NaC_4 at 10 GPa with orbital decomposition. The size of the symbols in (a) is proportional to the contribution of each orbital character. In (b), the total DOS is represented by the gray shaded region and the projected DOS corresponding to Na- s , C- p_z , and C- sp^2 orbitals is shown with red, green, and blue lines, respectively. (c) Band structure of C_4 structure (solid black) and Na structure (dashed red) with the same lattice parameters as NaC_4 . In (c), C_4 and Na bands are shifted downward and upward by ~ 2 eV to match the Fermi level of NaC_4 . (d) Charge density difference calculated using $\Delta\rho(r) = \rho_{\text{NaC}_4}(r) - \rho_{\text{C}_4}(r) - \rho_{\text{Na}}(r)$ and generated using VESTA [73]. The red and green lobes represent the charge accumulation and depletion regions, respectively, with an isosurface value set to $7 \times 10^{-2} e/\text{\AA}^3$.

only gains 0.11 electrons [63].

Figures 5(a)-5(d) illustrate the total and band-decomposed Fermi surface (FS). Comparison with the band structure in Fig. 4(a) reveals that the three bands crossing the Fermi level give rise to a multi-sheet FS structure. The FS sheets corresponding to band 1 (shown in blue) and band 2 (shown in green) exhibit 3D nested shapes and originate from the C- p_z states, as already pointed out in Ref. [15]. These nested regions surround two bean-shaped FS sheets (shown in red) centered around Γ of predominant Na- s character (band 3).

In Figs. 6(a) and 6(b), we plot the phonon dispersion and the atomic-projected phonon density of states (PhDOS). Similar to CaC_6 and several other GICs [63, 74, 76], the phonon dispersion can be divided into three regions: a low-frequency region composed of mostly Na-related vibrations mixed with out-of-plane C_z vibrations (< 30 meV), an intermediate frequency region dominated by out-of-plane C_z and Na_z vibrations ($30 - 80$ meV), and a high-frequency region of in-plane C_{xy} vibrations (> 100 meV).

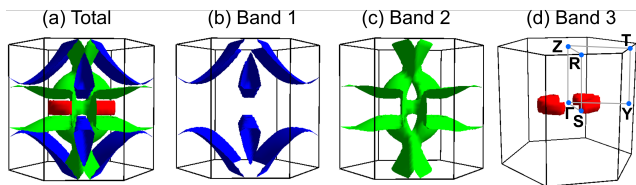


FIG. 5. (a) Fermi surface (FS) of NaC_4 at 10 GPa in the first Brillouin zone generated with FermiSurfer [75]. (b-d) Band decomposed FS corresponding to the three bands crossing E_F .

To investigate the e-ph interaction, we compute the isotropic Eliashberg spectral function $\alpha^2F(\omega)$ and the cumulative e-ph coupling strength $\lambda(\omega)$ shown in Fig. 6(c). Consistent with Ref. [15], we find that low- and intermediate-frequency phonons play a key role in achieving a high e-ph coupling in NaC_4 , and together they account for approximately 83% of the total $\lambda = 1.19$. Moreover, the relative contributions of these two sets of modes are very similar, with the e-ph coupling strengths associated primarily with Na and out-of-plane C_z vibrations making up 41% and 42% of λ , respectively. The corresponding breakdown of the total e-ph coupling strength into the three regions is illustrated by the horizontal dashed lines in Fig. 6(c). Notably, the high-frequency in-plane C_{xy} modes exhibit a significantly smaller contribution of only about 17%. This behavior is similar to other GICs (*i.e.*, CaC_6 , BaC_6 , SrC_6 [63, 67, 76, 77]) and Ca-intercalated bilayer graphene [67], where the largest contribution to λ has been associated with the modes below 80 meV.

The anisotropy in the e-ph coupling is quantified by evaluating the momentum-resolved $\lambda_{\mathbf{k}}$ as defined in Ref. [32]. Figure 7(a) clearly displays two peaks in the distribution of $\lambda_{\mathbf{k}}$, with a sharp peak centered around 1 and a small peak centered around 3. To further analyze the origin of these peaks, the variation of $\lambda_{\mathbf{k}}$ on the Fermi surface is shown in Fig. 7(b). According to the color map, the first sharp peak originates from the nested FS regions, while the second smaller peak arises from the Γ -centered FS regions. In particular, by comparing with the band structure and the band decomposed FS plots in Figs. 4(a) and 5, it becomes evident that the first peak arises from the coupling of the phonon modes with the

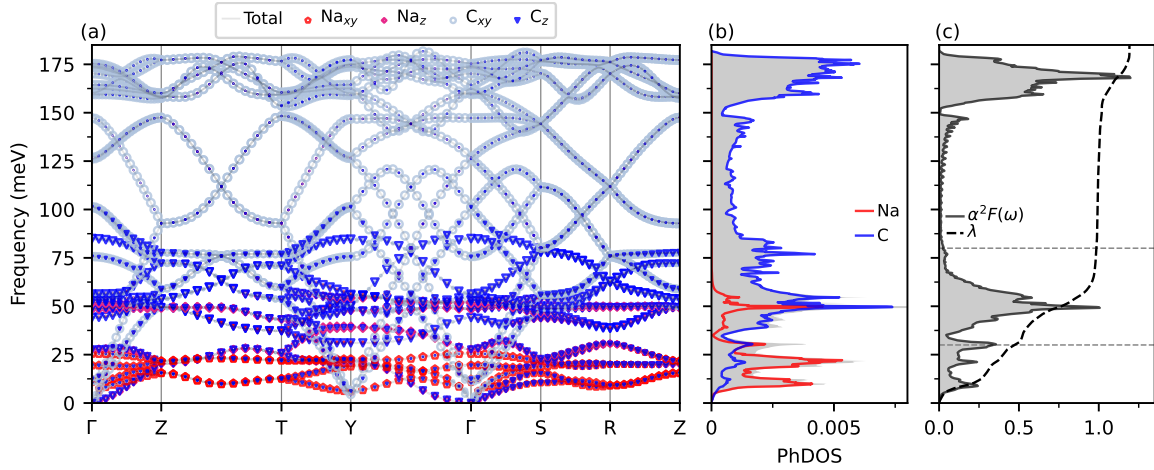


FIG. 6. (a) Phonon band structure of NaC_4 at 10 GPa with decomposition into in-plane and out-of-plane Na and C vibrations, respectively. The size of the symbols is proportional to the amount of vibration. (b) Total phonon density of states (PhDOS) (states/(meV·atom)) shown as the gray-shaded region along with atomic-projected PhDOS. (c) The isotropic Eliashberg spectral function $\alpha^2 F(\omega)$ and the cumulative electron-phonon coupling strength $\lambda(\omega)$.

$N(E_F)$ (states/(eV·spin·atom))	ω_{\log} (meV)	λ	μ^*	Semi-empirical T_c (K)		Isotropic ME T_c (K)			Anisotropic ME T_c (K)		
				AD	ML	FSR	FBW	FBW+ μ	FSR	FBW	FBW+ μ
0.10	33.85	1.19	0.1	34.9	43.3	43.5	45.5	45.5	47.0	48.2	48.2
			0.2	22.0	26.7	31.2	33.0	33.0	35.0	36.0	36.0

TABLE I. Summary of superconducting properties of NaC_4 at 10 GPa. The table lists the DOS at the Fermi level $N(E_F)$, the logarithmic phonon frequency ω_{\log} , the e-ph coupling strength λ , the Coulomb parameter μ^* , and the superconducting critical temperature T_c . The T_c values are calculated using different methodologies: the semi-empirical Allen-Dynes (AD) formula, the machine-learned (ML) model, the isotropic and anisotropic Fermi surface restricted (FSR) approximation, and the isotropic and anisotropic full bandwidth implementation without (FBW) and with (FBW+ μ) variation of the chemical potential μ .

C- π^* states (band 1 and band 2), while the second peak is mostly due to the intercalant Na- s states (band 3) with some contribution from the C- π^* states (band 2).

In order to determine the superconducting critical temperature, we solve the isotropic and anisotropic Migdal-Eliashberg equations [32, 33]. Since the electronic DOS strongly peaks close to E_F , we examine the superconducting gap using both the Fermi surface restricted (FSR) and the full bandwidth (FBW) approaches [33, 34]. In FSR, the DOS around E_F is assumed constant, whereas

in FBW the full energy dependence of the DOS is considered, allowing the inclusion of e-ph scattering processes away from E_F . A recent study has demonstrated the importance of the FBW treatment in the high-pressure H_3S and the low-pressure BaSiH_8 superconductors, which exhibit distinct DOS features that deviate significantly from the constant-DOS assumption made in the FSR approximation [34]. For a detailed description of the FSR and FBW approaches and their implementation in the EPW code, please see Refs. [32–34, and 56].

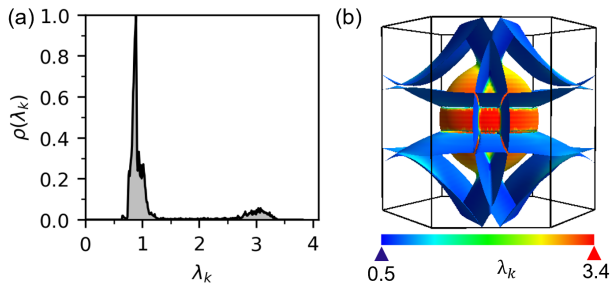


FIG. 7. (a) Distribution of the electron-phonon coupling strength λ_k . (b) Momentum-resolved electron-phonon coupling λ_k on the Fermi surface.

Figure 8(a) shows the isotropic superconducting gap Δ as a function of temperature, calculated with the FSR, FBW, and FBW+ μ methods using a Coulomb parameter $\mu^* = 0.1$ and 0.2. In FBW+ μ approach, we update the chemical potential self-consistently as discussed in Ref. [34]. Our calculations yield T_c values of 43.5 (31.2) K and 45.5 (33.0) K, and a zero-temperature superconducting gap of 7.62 (5.36) meV and 8.24 (5.70) meV for FSR and FBW with $\mu^* = 0.1$ (0.2), respectively. Furthermore, the superconducting gap versus temperature curves for FBW and FBW+ μ are basically identical, thus leading to the same T_c values. This can be understood as the Fermi level in NaC_4 lies slightly away from the vHS peak, as shown in Fig. 4(b), and therefore the DOS with and without updating μ are very similar. For compari-

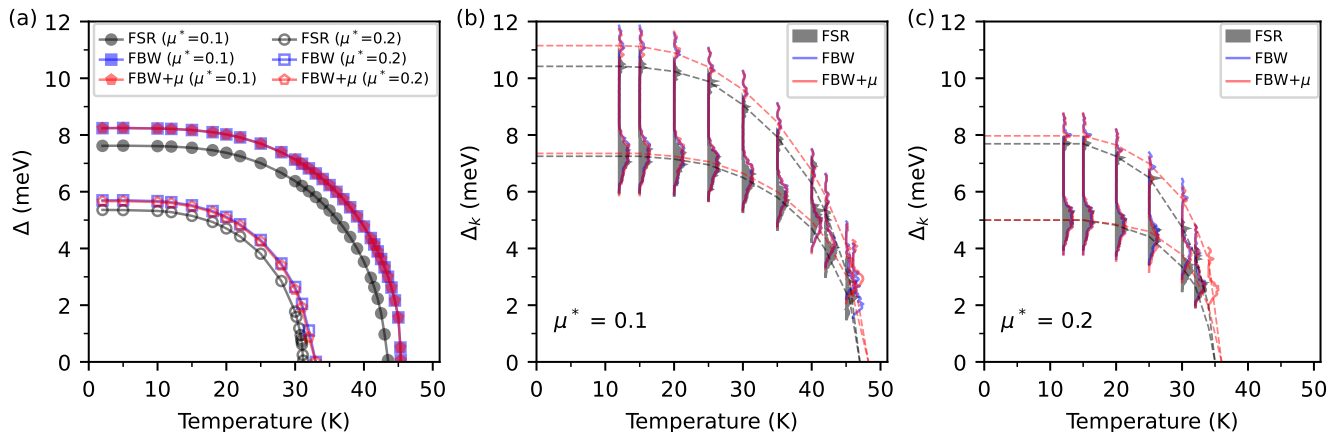


FIG. 8. (a) Isotropic superconducting gap of NaC₄ at 10 GPa as a function of temperature according to the FSR (gray), FBW (blue) and FBW+ μ (red) implementations of the Migdal-Eliashberg equations [33] for two different sets of Coulomb pseudopotential $\mu^* = 0.1$ and 0.2 . (b) and (c) Energy distribution of the anisotropic superconducting gap $\Delta_{\mathbf{k}}$ as a function of temperature for FSR (gray), FBW (blue) and FBW+ μ (red) approaches for $\mu^* = 0.1$ and 0.2 , respectively. The black dashed lines in (b) and (c) represent a guide for the eye highlighting the two superconducting gap distributions.

son, the commonly employed Allen-Dynes (AD) modified McMillan formula [16, 17] and the machine-learned (ML) SISSO model [78] give T_c values of 34.9 (22.0) K and 43.3 (26.7) K for $\mu^* = 0.1$ (0.2), respectively, with the latter producing results that match very well our isotropic predictions.

Given the anisotropy found in $\lambda_{\mathbf{k}}$, we calculate the anisotropic superconducting gap $\Delta_{\mathbf{k}}$ as a function of temperature shown in Figs. 8(b) and 8(c). We find two distinct gaps with mean values $\Delta_1 = 7.25$ (5.00) meV and $\Delta_2 = 10.42$ (7.69) meV for $\mu^* = 0.1$ (0.2) in the zero-temperature limit using the FSR approach. For comparison, CaC₆ displays a continuum anisotropic gap without separation into distinct gaps [67, 74, 77]. The Δ_1 gap is highly anisotropic and varies over a wide energy range of 1.75 meV. In contrast, the Δ_2 gap is less pronounced (*i.e.*, fewer energy states contribute to this gap) and has a much narrower distribution of only 0.75 meV. The superconducting T_c is estimated to be 47.0 (35.0) K for $\mu^* = 0.1$ (0.2), about 8 % (12 %) higher than the isotropic FSR value. Application of the FBW and FBW+ μ treatment only shifts slightly the gap distribution to higher energies while retaining the overall shape at each temperature. The resulting T_c using the two FBW approaches is estimated to be 48.2 (36.0) K with $\mu^* = 0.1$ (0.2). The T_c values obtained with different approaches are summarized in Table I.

Figure 9(a) shows the momentum-resolved superconducting gap $\Delta_{\mathbf{k}}$ on the FS at 12 K within the FSR approximation using $\mu^* = 0.1$. Comparing this with Fig. 7(b), the regions of the FS with the lower gap $\Delta_1 = 7.35$ meV can be associated with the C- π^* states (band 1 and band 2). In contrast, the upper gap $\Delta_2 = 10.60$ meV primarily arises from the Na- s states (band 3) with some contribution from the C- π^* states (band 2). Similarly,

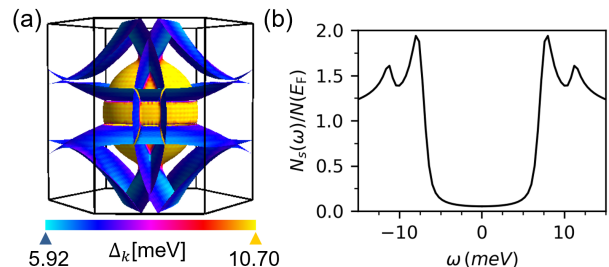


FIG. 9. (a) Momentum-resolved superconducting gap $\Delta_{\mathbf{k}}$ on the Fermi surface and (b) normalized quasiparticle DOS for NaC₄ at 12 K and 10 GPa using the FSR approach with $\mu^* = 0.1$. The data points in (b) correspond to electronic states within ± 0.2 eV from the Fermi energy.

in CaC₆, the smallest and highest values of the smeared multi-gap structure have been associated with the C- π^* and Ca- s, d_{z^2} states [74, 77]. The two-gap structure of NaC₄ is also evident from the corresponding quasiparticle DOS plotted in Fig. 9(b).

Finally, we explore the effect of electron and hole doping on the T_c in the light of the vHS peak present in the DOS of NaC₄ near the Fermi level (see Fig. 10(a)). Previous theoretical studies on H₃S have shown an enhancement in T_c when the Fermi level approaches the maximum of the vHS peak [34, 79, 80]. To investigate the dependence of T_c with doping, we shift the Fermi level by $\Delta\varepsilon_F$ in the -0.2 eV to 0.1 eV range in increments of 0.05 eV, corresponding to changes in the electron number of ~ 0.076 . Figure 10(b) shows the T_c values obtained by solving the isotropic and anisotropic ME equations within the FSR and FBW approaches, and those obtained with the semi-empirical AD and ML formulas. Overall, all treatments produce a similar trend for the

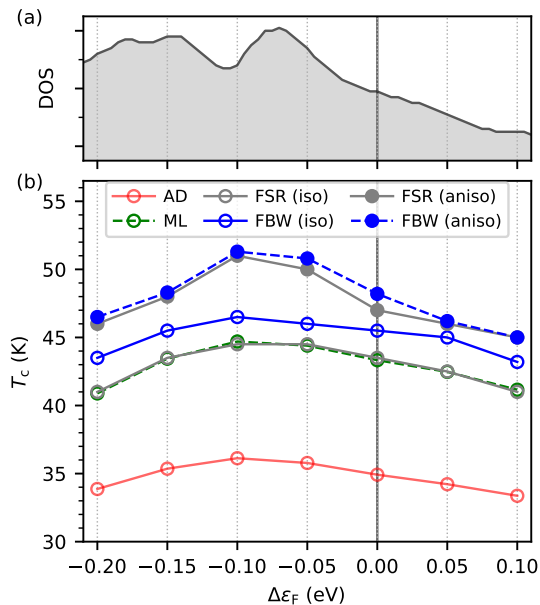


FIG. 10. (a) Total DOS (states/(eV·spin·atom)) of NaC_4 in the energy range of -0.2 to 0.1 eV. (b) Superconducting critical temperature T_c as a function of Fermi level shift $\Delta\varepsilon_F$ obtained with the AD formula, the ML model, and the isotropic and anisotropic ME equations in the FSR and FBW approaches with a $\mu^* = 0.1$.

variation of T_c with doping. In particular, the T_c versus $\Delta\varepsilon_F$ curve obtained with the anisotropic approach resembles the shape dependence of the DOS, the T_c reaching a maximum value at $\Delta\varepsilon_F = -0.1$ eV when the Fermi level lies in very close proximity to the vHS peak. For comparison, the effect of doping on T_c is less pronounced when employing the isotropic ME treatment or the semi-empirical formulas, with the AD formula consistently underestimating the T_c values by about 7 K.

IV. SUMMARY

We have explored the stability and superconductivity of Na-intercalated graphite compounds under moderate pressures using *ab initio* methods. Through systematic screening, we identified new stable stoichiometries, Na_3C_{10} , NaC_8 , NaC_{10} , and NaC_{12} , which redefine the previously established convex hulls up to 10 GPa. While some compounds may lack stability at zero temperature, they could be high-temperature ground states or form through cold compression of graphite. Our analysis of the nearly free electron states important for superconductivity in intercalated compounds narrows down the promising candidates to two. One of them, NaC_4 proposed previously by Hao *et al.* [15], has been re-analyzed within the anisotropic Migdal-Eliashberg theory and predicted to be a two-gap superconductor with a T_c of 48 K, 24% above the prior isotropic Eliashberg estimate. The other compound, Na_3C_{10} introduced in the present study, appears to be prone to interlayer shifts and may develop domain walls to become dynamically stable. According to our estimates, it should have T_c at least comparable to that in NaC_4 at 10 GPa. The *ab initio* findings reveal the Na-C system may host viable compounds with unexpectedly high T_c for electron-doped materials.

ACKNOWLEDGMENTS

S.B.M. and E.R.M. acknowledge support from the National Science Foundation (NSF) Award No. DMR-2035518. E.T.M. and A.N.K. acknowledge support from the NSF Award No. DMR-2320073. This study used the Frontera supercomputer at the Texas Advanced Computing Center through the Leadership Resource Allocation (LRAC) award DMR22004. Frontera is made possible by NSF award OAC-1818253 [81]. This study also used the Expanse system at the San Diego Supercomputer Center through allocation TG-DMR180071 from the Advanced Cyberinfrastructure Coordination Ecosystem: Services & Support (ACCESS) program [82], which is supported by NSF grants #2138259, #2138286, #2138307, #2137603, and #2138296.

-
- [1] R. A. Jishi and M. S. Dresselhaus, Superconductivity in graphite intercalation compounds, *Phys. Rev. B* **45**, 12465 (1992).
 - [2] E. Ekimov, V. Sidorov, E. Bauer, N. Mel'Nik, N. Curro, J. Thompson, and S. Stishov, Superconductivity in diamond, *Nature* **428**, 542 (2004).
 - [3] H. Okazaki, T. Wakita, T. Muro, T. Nakamura, Y. Muraoka, T. Yokoya, S.-i. Kurihara, H. Kwarada, T. Oguchi, and Y. Takano, Signature of high T_c above 25 K in high quality superconducting diamond, *Appl. Phys. Lett.* **106**, 052601 (2015).
 - [4] S. Heguri, N. Kawade, T. Fujisawa, A. Yamaguchi, A. Sumiyama, K. Tanigaki, and M. Kobayashi, Superconductivity in the graphite intercalation compound BaC_6 , *Phys. Rev. Lett.* **114**, 247201 (2015).
 - [5] H. Zhou, T. Xie, T. Taniguchi, K. Watanabe, and A. F. Young, Superconductivity in rhombohedral trilayer graphene, *Nature* **598**, 434 (2021).
 - [6] A. Bhaumik, R. Sachan, S. Gupta, and J. Narayan, Discovery of high-temperature superconductivity ($T_c = 55$ K) in B-doped Q-Carbon, *ACS Nano* **11**, 11915 (2017).
 - [7] N. Emery, C. Hérold, J.-F. Marêché, and P. Lagrange, Synthesis and superconducting properties of CaC_6 , *Sci.*

- Technol. Adv. Mater.* **9**, 044102 (2008).
- [8] M. Dresselhaus and G. Dresselhaus, Intercalation compounds of graphite, *Adv. Phys.* **30**, 139 (1981).
- [9] N. B. Hannay, T. H. Geballe, B. T. Matthias, K. Andres, P. Schmidt, and D. MacNair, Superconductivity in graphitic compounds, *Phys. Rev. Lett.* **14**, 225 (1965).
- [10] T. E. Weller, M. Ellerby, S. S. Saxena, R. P. Smith, and N. T. Skipper, Superconductivity in the intercalated graphite compounds C_6Yb and C_6Ca , *Nat. Phys.* **1**, 39 (2005).
- [11] N. Emery, C. Hérold, M. d’Astuto, V. Garcia, C. Bellin, J. F. Marêché, P. Lagrange, and G. Loupiau, Superconductivity of bulk CaC_6 , *Phys. Rev. Lett.* **95**, 087003 (2005).
- [12] I. Belash, A. Bronnikov, O. Zharikov, and A. Pal’nichenko, Superconductivity of graphite intercalation compound with lithium C_2Li , *Solid State Commun.* **69**, 921 (1989).
- [13] I. Belash, A. Bronnikov, O. Zharikov, and A. Pal’nichenko, On the superconductivity of graphite intercalation compounds with sodium, *Solid State Commun.* **64**, 1445 (1987).
- [14] A. Gauzzi, S. Takashima, N. Takeshita, C. Terakura, H. Takagi, N. Emery, C. Hérold, P. Lagrange, and G. Loupiau, Enhancement of superconductivity and evidence of structural instability in intercalated graphite C_6Ca under high pressure, *Phys. Rev. Lett.* **98**, 067002 (2007).
- [15] C.-M. Hao, X. Li, A. R. Oganov, J. Hou, S. Ding, Y. Ge, L. Wang, X. Dong, H.-T. Wang, G. Yang, X.-F. Zhou, and Y. Tian, Superconductivity in compounds of sodium-intercalated graphite, *Phys. Rev. B* **108**, 214507 (2023).
- [16] W. L. McMillan, Transition temperature of strong-coupled superconductors, *Phys. Rev.* **167**, 331 (1968).
- [17] P. B. Allen and R. C. Dynes, Transition temperature of strong-coupled superconductors reanalyzed, *Phys. Rev. B* **12**, 905 (1975).
- [18] A. R. Oganov, *Modern Methods of Crystal Structure Prediction* (John Wiley & Sons, 2011).
- [19] A. R. Oganov, C. J. Pickard, Q. Zhu, and R. J. Needs, Structure prediction drives materials discovery, *Nat Rev Mater* **4**, 331 (2019).
- [20] Y. Wang and Y. Ma, Perspective: Crystal structure prediction at high pressures, *The Journal of Chemical Physics* **140**, 040901 (2014).
- [21] L. Boeri and *et al.*, The 2021 room-temperature superconductivity roadmap, *J. Phys.: Condens. Matter* **34**, 183002 (2022).
- [22] A. N. Kolmogorov, S. Shah, E. R. Margine, A. F. Bialon, T. Hammerschmidt, and R. Drautz, New superconducting and semiconducting Fe-B compounds predicted with an ab initio evolutionary search, *Phys. Rev. Lett.* **105**, 217003 (2010).
- [23] A. N. Kolmogorov, S. Shah, E. R. Margine, A. K. Kleppe, and A. P. Jephcoat, Pressure-driven evolution of the covalent network in CaB_6 , *Phys. Rev. Lett.* **109**, 075501 (2012).
- [24] S. Hajinazar, A. Thorn, E. D. Sandoval, S. Kharabadze, and A. N. Kolmogorov, MAISE: Construction of neural network interatomic models and evolutionary structure optimization, *Comput. Phys. Commun.* **259**, 107679 (2021).
- [25] S. Shah and A. N. Kolmogorov, Stability and superconductivity of Ca-B phases at ambient and high pressure, *Phys. Rev. B* **88**, 014107 (2013).
- [26] S. Kharabadze, A. Thorn, E. A. Koulakova, and A. N. Kolmogorov, Prediction of stable Li-Sn compounds: boosting ab initio searches with neural network potentials, *npj Comput Mater* **8**, 1 (2022).
- [27] J. Singh, A. Behatha, S. Kharabadze, A. N. Kolmogorov, G. Vaitheeswaran, and V. Kanchana, Prediction of ground state structures and robust Weyl fermionic states in MnRhP, *J. Phys. Chem. C* **126**, 17328 (2022).
- [28] C. R. Tomassetti, G. P. Kafle, E. T. Marcial, E. R. Margine, and A. N. Kolmogorov, Prospect of high-temperature superconductivity in layered metal borocarbides, *J. Mater. Chem. C* **12**, 4870 (2024).
- [29] S. Kharabadze, M. Meyers, C. R. Tomassetti, E. R. Margine, I. I. Mazin, and A. N. Kolmogorov, Thermodynamic stability of Li-B-C compounds from first principles, *Phys. Chem. Chem. Phys.* **25**, 7344 (2023).
- [30] J. Klimeš, D. R. Bowler, and A. Michaelides, Chemical accuracy for the van der waals density functional, *J. Phys.: Condensed Matter* **22**, 022201 (2009).
- [31] J. Klimeš, D. R. Bowler, and A. Michaelides, Van der waals density functionals applied to solids, *Phys. Rev. B* **83**, 195131 (2011).
- [32] E. R. Margine and F. Giustino, Anisotropic Migdal-Eliashberg theory using Wannier functions, *Phys. Rev. B* **87**, 024505 (2013).
- [33] H. Lee, S. Poncé, K. Bushick, S. Hajinazar, J. Lafuente-Bartolome, J. Leveillee, C. Lian, J.-M. Lihm, F. Macheda, H. Mori, H. Paudyal, W. H. Sio, S. Tiwari, M. Zacharias, X. Zhang, N. Bonini, E. Kioupakis, E. R. Margine, and F. Giustino, Electron-phonon physics from first principles using the EPW code, *npj Comput. Mater.* **9**, 2057 (2023).
- [34] R. Lucrezi, P. P. Ferreira, S. Hajinazar, H. Mori, H. Paudyal, E. R. Margine, and C. Heil, Full-bandwidth anisotropic migdal-eliasberg theory and its application to superhydrides, *Commun. Phys.* **7**, 33 (2024).
- [35] A. Y. Liu, I. I. Mazin, and J. Kortus, Beyond Eliashberg Superconductivity in MgB_2 : Anharmonicity, Two-Phonon Scattering, and Multiple Gaps, *Phys. Rev. Lett.* **87**, 087005 (2001).
- [36] H. J. Choi, D. Roundy, H. Sun, M. L. Cohen, and S. G. Louie, The origin of the anomalous superconducting properties of MgB_2 , *Nature* **418**, 758 (2002).
- [37] H. J. Choi, S. G. Louie, and M. L. Cohen, Prediction of superconducting properties of CaB_2 using anisotropic eliasberg theory, *Phys. Rev. B* **80**, 064503 (2009).
- [38] G. P. Kafle, C. R. Tomassetti, I. I. Mazin, A. N. Kolmogorov, and E. R. Margine, Ab initio study of Li-Mg-B superconductors, *Phys. Rev. Mater.* **6**, 084801 (2022).
- [39] J. Wang, M. Wang, X. Liu, M. Jiang, and L. Liu, Covalent bond inducing strong electron-phonon coupling superconductivity in MgB_2 -type transition metal diboride WB_2 , *Phys. Rev. Mater.* **7**, 074804 (2023).
- [40] C. R. Tomassetti, G. P. Kafle, E. T. Marcial, E. R. Margine, and A. N. Kolmogorov, Prospect of high-temperature superconductivity in layered metal borocarbides, *J. Mater. Chem. C* **12**, 4870 (2024).
- [41] G. Kresse and J. Furthmüller, Efficient iterative schemes for ab initio total-energy calculations using a plane-wave basis set, *Phys. Rev. B* **54**, 11169 (1996).
- [42] P. E. Blöchl, Projector augmented-wave method, *Phys. Rev. B* **50**, 17953 (1994).

- [43] J. W. Furness, A. D. Kaplan, J. Ning, J. P. Perdew, and J. Sun, Accurate and Numerically Efficient r^2 SCAN Meta-Generalized Gradient Approximation, *J. Phys. Chem. Lett.* **11**, 8208 (2020).
- [44] J. Ning, M. Kothakonda, J. W. Furness, A. D. Kaplan, S. Ehlert, J. G. Brandenburg, J. P. Perdew, and J. Sun, Workhorse minimally empirical dispersion-corrected density functional with tests for weakly bound systems: r^2 SCAN+rVV10, *Phys. Rev. B* **106**, 075422 (2022).
- [45] A. Togo and I. Tanaka, First principles phonon calculations in materials science, *Scr. Mater.* **108**, 1 (2015).
- [46] See Supplemental Material for detailed figures and structural information. Figures S1 and S2 illustrate the distance to the convex hull for selected Na-C phases using optB86b-vdW and optB88-vdW functionals. Figure S3 presents the stability analysis using r^2 SCAN+rVV10 functional. Figure S4 shows the electronic structure and phonon dispersion of selected stable structures calculated using Quantum ESPRESSO. Figure S5 shows the phonon dispersion of oP104 calculated using PHONOPY and VASP. CIF files for select Na-C phases are also included.
- [47] P. Giannozzi and *et al.*, Advanced capabilities for materials modelling with Quantum ESPRESSO, *J. Phys.: Condens. Matter* **29**, 465901 (2017).
- [48] T. Thonhauser, S. Zuluaga, C. A. Arter, K. Berland, E. Schröder, and P. Hyldgaard, Spin signature of nonlocal correlation binding in metal-organic frameworks, *Phys. Rev. Lett.* **115**, 136402 (2015).
- [49] K. Berland, V. R. Cooper, K. Lee, E. Schröder, T. Thonhauser, P. Hyldgaard, and B. I. Lundqvist, van der Waals forces in density functional theory: a review of the vdW-DF method, *Rep. Prog. Phys.* **78**, 066501 (2015).
- [50] D. R. Hamann, Optimized norm-conserving vanderbilt pseudopotentials, *Phys. Rev. B* **88**, 085117 (2013).
- [51] M. van Setten, M. Giantomassi, E. Bousquet, M. Verstraete, D. Hamann, X. Gonze, and G.-M. Rignanese, The PseudoDojo: Training and grading a 85 element optimized norm-conserving pseudopotential table, *Comput. Phys. Commun.* **226**, 39 (2018).
- [52] J. P. Perdew, K. Burke, and M. Ernzerhof, Generalized gradient approximation made simple, *Phys. Rev. Lett.* **77**, 3865 (1996).
- [53] M. Methfessel and A. T. Paxton, High-precision sampling for brillouin-zone integration in metals, *Phys. Rev. B* **40**, 3616 (1989).
- [54] S. Baroni, S. de Gironcoli, A. Dal Corso, and P. Giannozzi, Phonons and related crystal properties from density-functional perturbation theory, *Rev. Mod. Phys.* **73**, 515 (2001).
- [55] F. Giustino, M. L. Cohen, and S. G. Louie, Electron-phonon interaction using Wannier functions, *Phys. Rev. B* **76**, 165108 (2007).
- [56] S. Poncé, E. Margine, C. Verdi, and F. Giustino, EPW: Electron-phonon coupling, transport and superconducting properties using maximally localized Wannier functions, *Comput. Phys. Commun.* **209**, 116 (2016).
- [57] N. Marzari, A. A. Mostofi, J. R. Yates, I. Souza, and D. Vanderbilt, Maximally localized Wannier functions: Theory and applications, *Rev. Mod. Phys.* **84**, 1419 (2012).
- [58] G. Pizzi and *et al.*, Wannier90 as a community code: new features and applications, *J. Phys. Condens. Matter* **32**, 165902 (2020).
- [59] B. Sundqvist, Carbon under pressure, *Phys. Rep.* **909** (2021).
- [60] A. N. Kolmogorov and S. Curtarolo, Prediction of different crystal structure phases in metal borides: A lithium monoboride analog to MgB_2 , *Phys. Rev. B* **73**, 180501(R) (2006).
- [61] E. D. Sandoval, S. Hajinazar, and A. N. Kolmogorov, Stability of two-dimensional BN-Si structures, *Phys. Rev. B* **94**, 094105 (2016).
- [62] A. N. Kolmogorov, S. Hajinazar, C. Angyal, V. L. Kuznetsov, and A. P. Jephcoat, Synthesis of a predicted layered LiB via cold compression, *Phys. Rev. B* **92**, 144110 (2015).
- [63] M. Calandra and F. Mauri, Theoretical explanation of superconductivity in C_6Ca , *Phys. Rev. Lett.* **95**, 237002 (2005).
- [64] G. Csányi, P. B. Littlewood, A. H. Nevidomskyy, C. J. Pickard, and B. D. Simons, The role of the interlayer state in the electronic structure of superconducting graphite intercalated compounds, *Nat. Phys.* **1**, 42 (2005).
- [65] I. I. Mazin, Intercalant-driven superconductivity in YbC_6 and CaC_6 , *Phys. Rev. Lett.* **95**, 227001 (2005).
- [66] I. Mazin and A. Balatsky, Superconductivity in Ca-intercalated bilayer graphene, *Philos. Mag. Lett.* **90**, 731 (2010).
- [67] E. Margine, H. Lambert, and F. Giustino, Electron-phonon interaction and pairing mechanism in superconducting Ca-intercalated bilayer graphene, *Sci. Rep.* **6**, 21414 (2016).
- [68] G. Profeta, M. Calandra, and F. Mauri, Phonon-mediated superconductivity in graphene by lithium deposition, *Nat. Phys.* **8**, 131 (2012).
- [69] J.-J. Zheng and E. R. Margine, First-principles calculations of the superconducting properties in Li-decorated monolayer graphene within the anisotropic migdal-eliasberg formalism, *Phys. Rev. B* **94**, 064509 (2016).
- [70] M. Calandra, A. N. Kolmogorov, and S. Curtarolo, Search for high T_c in layered structures: The case of LiB, *Phys. Rev. B* **75**, 144506 (2007).
- [71] L. Boeri, G. B. Bachelet, M. Giantomassi, and O. K. Andersen, Electron-phonon interaction in graphite intercalation compounds, *Phys. Rev. B* **76**, 064510 (2007).
- [72] E. R. Margine and V. H. Crespi, Universal behavior of nearly free electron states in carbon nanotubes, *Phys. Rev. Lett.* **96**, 196803 (2006).
- [73] K. Momma and F. Izumi, *VESTA3* for three-dimensional visualization of crystal, volumetric and morphology data, *J. Appl. Cryst.* **44**, 1272 (2011).
- [74] A. Sanna, S. Pittalis, J. K. Dewhurst, M. Monni, S. Sharma, G. Ummarino, S. Massidda, and E. K. U. Gross, Phononic self-energy effects and superconductivity in CaC_6 , *Phys. Rev. B* **85**, 184514 (2012).
- [75] M. Kawamura, FermiSurfer: Fermi-surface viewer providing multiple representation schemes, *Comput. Phys. Commun.* **239**, 197 (2019).
- [76] M. Calandra and F. Mauri, Possibility of superconductivity in graphite intercalated with alkaline earths investigated with density functional theory, *Phys. Rev. B* **74**, 094507 (2006).
- [77] A. Sanna, G. Profeta, A. Floris, A. Marini, E. K. U. Gross, and S. Massidda, Anisotropic gap of superconducting CaC_6 : A first-principles density functional calculation, *Phys. Rev. B* **75**, 020511(R) (2007).

- [78] S. Xie, Y. Quan, A. Hire, B. Deng, J. DeStefano, I. Salinas, U. Shah, L. Fanfarillo, J. Lim, J. Kim, *et al.*, Machine learning of superconducting critical temperature from Eliashberg theory, *npj Comput. Mater.* **8**, 14 (2022).
- [79] W. Sano, T. Koretsune, T. Tadano, R. Akashi, and R. Arita, Effect of Van Hove singularities on high- T_c superconductivity in H_3S , *Phys. Rev. B* **93**, 094525 (2016).
- [80] Y. Quan and W. E. Pickett, Van Hove singularities and spectral smearing in high-temperature superconducting H_3S , *Phys. Rev. B* **93**, 104526 (2016).
- [81] D. Stanzione, J. West, R. T. Evans, T. Minyard, O. Ghattas, and D. K. Panda, Frontera: The Evolution of Leadership Computing at the National Science Foundation, in *Practice and Experience in Advanced Research Computing* (ACM, New York, NY, USA, 2020) pp. 106–111.
- [82] T. J. Boerner, S. Deems, T. R. Furlani, S. L. Knuth, and J. Towns, ACCESS: Advancing Innovation: NSF’s Advanced Cyberinfrastructure Coordination Ecosystem: Services & Support, in *Practice and Experience in Advanced Research Computing*, PEARC ’23 (Association for Computing Machinery, New York, NY, USA, 2023) p. 173–176.
-

Supplemental Material:
Stability-superconductivity map for compressed Na-intercalated graphite

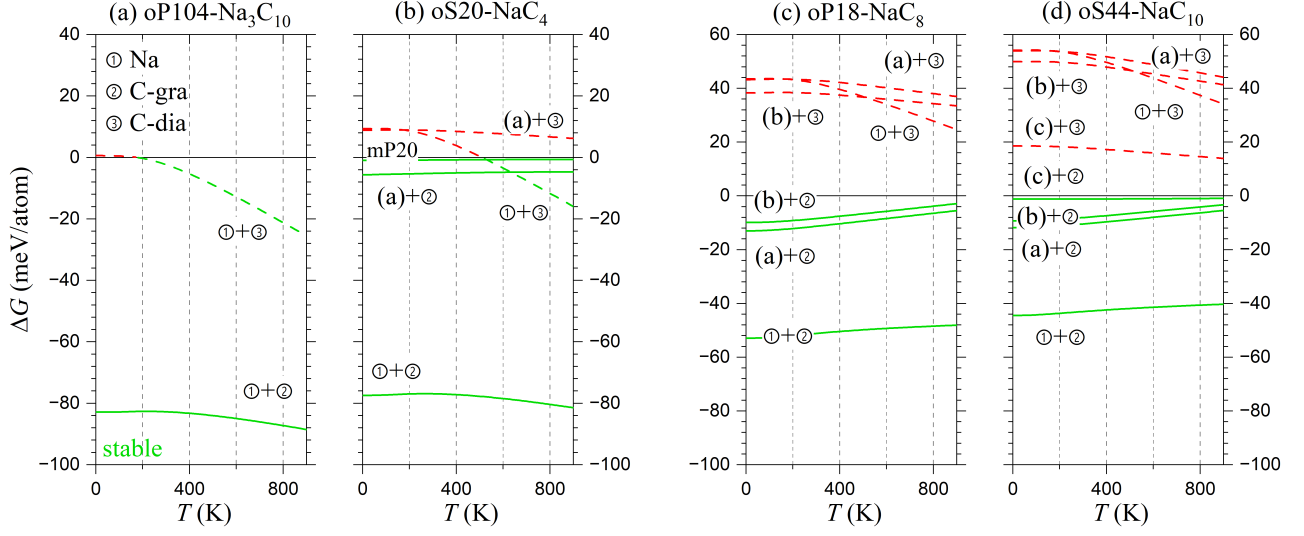


FIG. S1. Relative Gibbs free energy at 10 GPa as a function of temperature for select Na-C phases calculated with the optB86b-vdW functional. Each line shows relative stability with respect to a combination of known (circled numbers) or proposed (bracketed letters) phases. The dashed lines correspond to phase combinations containing the diamond ground state at this pressure, which we argue to be not relevant for Na intercalation of graphite via cold compression. Since all solid lines measuring the relative stability with respect to graphite are below zero (shown in green), all four proposed phases are expected to be synthesizable in the considered temperature range. In addition, oP104-Na₃C₁₀ is globally stable above about 200 K.

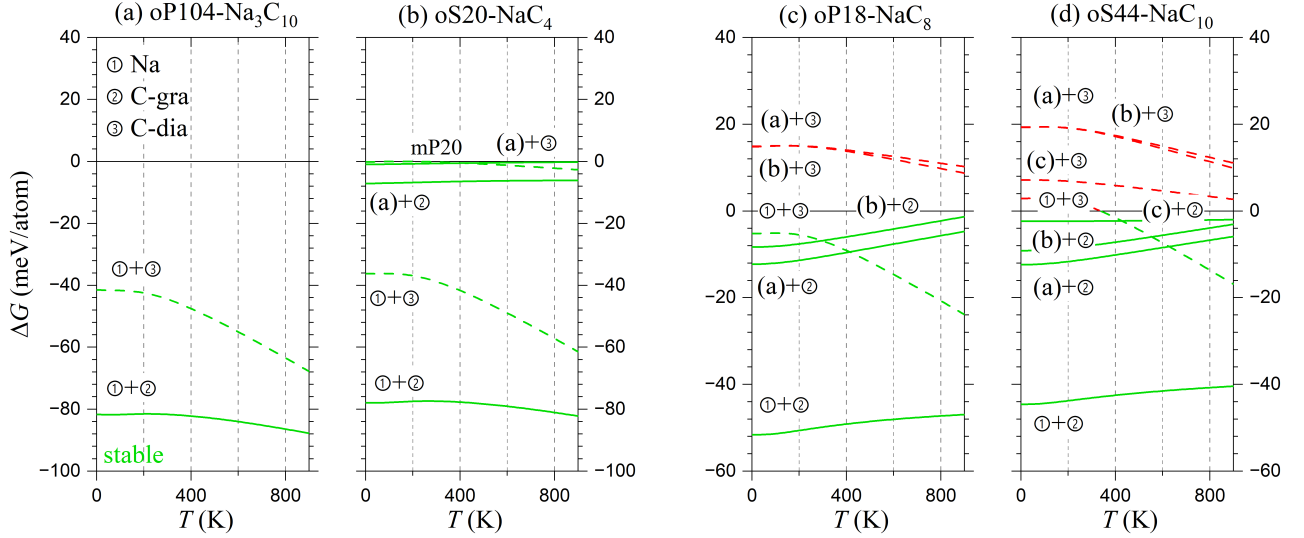


FIG. S2. Relative Gibbs free energy at 10 GPa as a function of temperature for select Na-C phases calculated with the optB88-vdW functional (see Fig. S1 caption for further details). All four phases appear synthesizable in the considered temperature range if graphite is used as a starting material, with two of them, oP104-Na₃C₁₀ and oS20-NaC₄, being globally stable with respect to diamond.

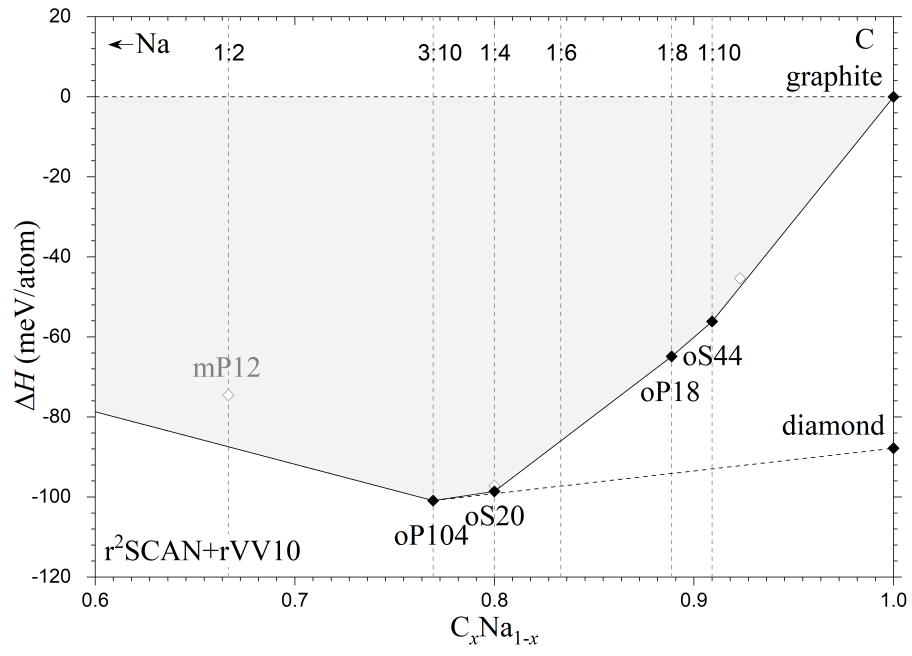


FIG. S3. Stability of C-Na phases at 10 GPa and 0 K calculated with the $r^2\text{SCAN}+r\text{VV10}$ functional [44]. The global (local) convex hulls are denoted with solid (dashed) lines. The set of four locally stable phases is consistent with those obtained with the optB88-vdW and optB86b-vdW functionals (see Fig. 2 in the manuscript).

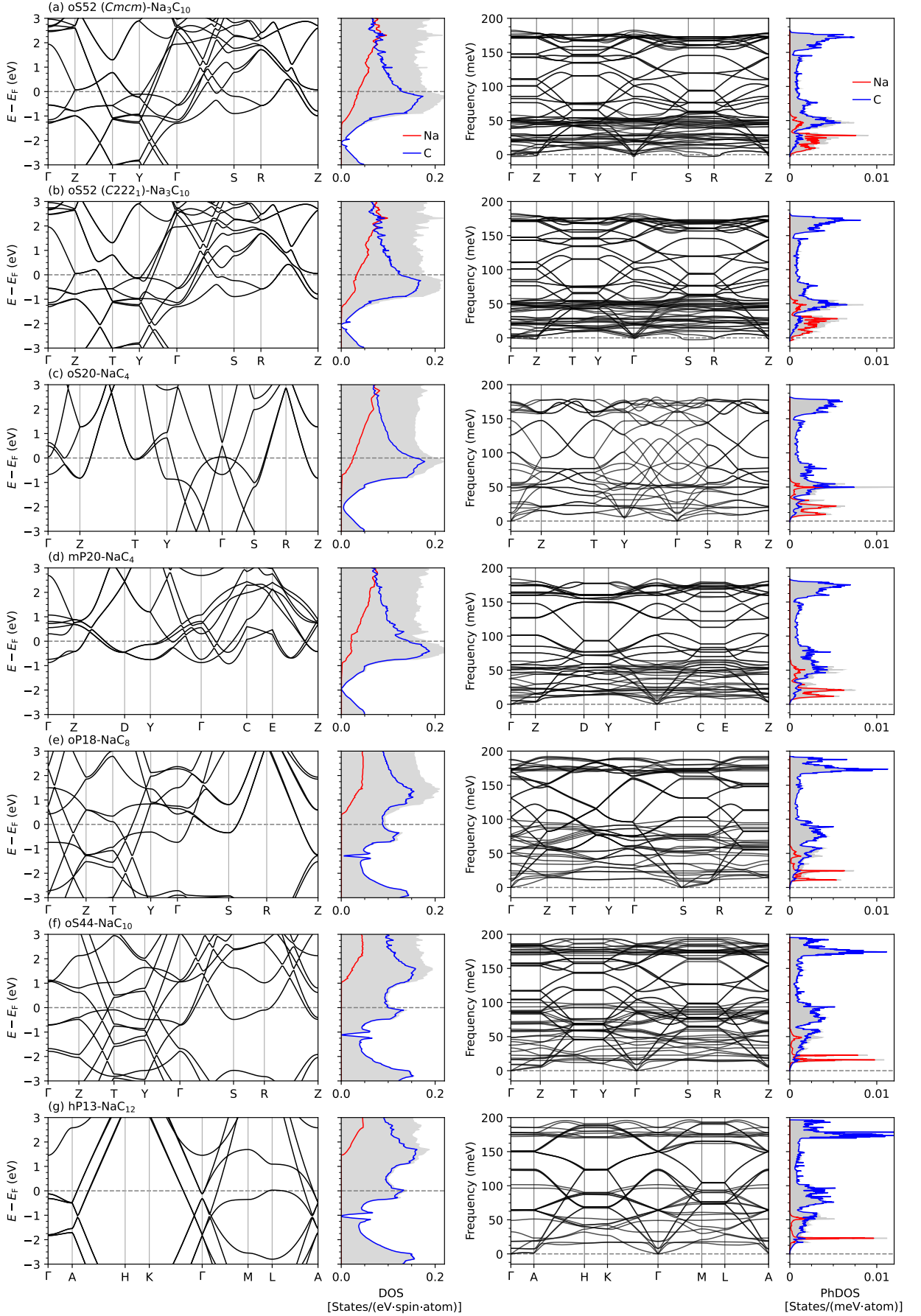


FIG. S4. Electronic band structures, DOS, phonon dispersion, and PhDOS calculated with Quantum ESPRESSO for (a) oS52 ($Cmcm$)- Na_3C_{10} , (b) oS52 ($C222_1$)- Na_3C_{10} , (c) oS20- NaC_4 , (d) mP20- NaC_4 , (e) oP18- NaC_8 , (f) oS44- NaC_{10} , and (g) hP13- NaC_{12} at 10 GPa.

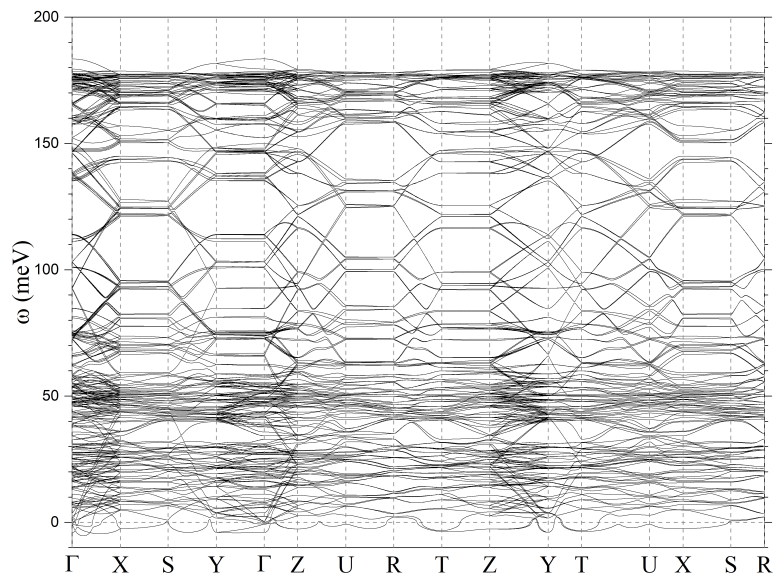


FIG. S5. Phonon dispersion for oP104-Na₃C₁₀ at 10 GPa calculated with the finite displacement method using PHONOPY and VASP. The linear response calculations proved to be particularly demanding in this case.

Listing 1. CIF file for mP12-NaC₂ containing the VASP optimized lattice constants and atomic positions at 5 GPa.

```
_symmetry_Int_Tables_number 11
_cell_length_a 4.9727911481359230
_cell_length_b 4.3033130471733356
_cell_length_c 7.2283164338578878
_cell_angle_alpha 90.000000000000000
_cell_angle_beta 98.7971251687718848
_cell_angle_gamma 90.000000000000000
_symmetry_Int_Tables_number 11
_chemical_formula_sum
'C Na '
loop_
_atom_site_label
_atom_site_type_symbol
_atom_site_site_symmetry_multiplicity
_atom_site_occupancy wyckoff
_atom_site_fract_x
_atom_site_fract_y
_atom_site_fract_z
C1 C 4 f 0.3739409661740112 0.9170379731911351 0.9946890523514327
C2 C 4 f 0.8750958655346466 0.9166666666666666 0.0006343559857812
Na1 Na 2 e 0.5359695585021954 0.2500000000000000 0.6650636316635571
Na2 Na 2 e 0.0402706172980845 0.7500000000000000 0.6740356198602769
#End
```

Listing 2. CIF file for oS52-Na₃C₁₀ (*Cmcm*) containing the VASP optimized lattice constants and atomic positions at 10 GPa.

```

_symmetry_Int_Tables_number 63
_cell_length_a 4.3345876014862990
_cell_length_b 12.4744252875898436
_cell_length_c 8.6445697968283355
_cell_angle_alpha 90.000000000000000
_cell_angle_beta 90.000000000000000
_cell_angle_gamma 90.000000000000000
_symmetry_Int_Tables_number 63
_chemical_formula_sum
'C Na '
loop_
_atom_site_label
_atom_site_type_symbol
_atom_site_site_symmetry_multiplicity
_atom_site_occupancy wyckoff
_atom_site_fract_x
_atom_site_fract_y
_atom_site_fract_z
C1 C 16 h 0.8333333333333334 0.2001572180448292 0.9922351866168100
C2 C 16 h 0.3333333333333333 0.1000940496660334 0.5120353617970680
C3 C 8 e 0.1669435501513448 0.0000000000000000 0.5000000000000000
Na1 Na 4 c 0.5000000000000000 0.2484765693898439 0.7500000000000000
Na2 Na 4 c 0.5000000000000000 0.4049998440550624 0.2500000000000000
Na3 Na 4 c 0.0000000000000000 0.4420250481179195 0.7500000000000000
#End

```

Listing 3. CIF file for oS52-Na₃C₁₀ (*C222₁*) containing the VASP optimized lattice constants and atomic positions at 10 GPa.

```

_symmetry_Int_Tables_number 20
_cell_length_a 4.3283454520037719
_cell_length_b 12.4550961726904426
_cell_length_c 8.7019554570706106
_cell_angle_alpha 90.000000000000000
_cell_angle_beta 90.000000000000000
_cell_angle_gamma 90.000000000000000
_symmetry_Int_Tables_number 20
_chemical_formula_sum
'C Na '
loop_
_atom_site_label
_atom_site_type_symbol
_atom_site_site_symmetry_multiplicity
_atom_site_occupancy wyckoff
_atom_site_fract_x
_atom_site_fract_y
_atom_site_fract_z
C1 C 8 c 0.8565797045459753 0.2003656544749290 0.9906896905986997
C2 C 8 c 0.3098836960032756 0.1001369377800074 0.5094431237821340
C3 C 4 a 0.1436128152677867 0.0000000000000000 0.5000000000000000
C4 C 8 c 0.6902220277336751 0.3001567132545233 0.0045171073435595
C5 C 8 c 0.1433277497844330 0.4001932826437908 0.4831244691225791
C6 C 4 a 0.8096430435082667 0.0000000000000000 0.5000000000000000
Na1 Na 4 b 0.5000000000000000 0.0695855689837757 0.2500000000000000
Na2 Na 4 b 0.5000000000000000 0.2418185439696074 0.7500000000000000
Na3 Na 4 b 0.5000000000000000 0.4098049512768895 0.2500000000000000
#End

```

Listing 4. CIF file for oP104-Na₃C₁₀ containing the VASP optimized lattice constants and atomic positions at 10 GPa.

```

_symmetry_Int_Tables_number 19
_cell_length_a 8.6571339789676092
_cell_length_b 8.7003343806980844
_cell_length_c 12.4566915428260288
_cell_angle_alpha 90.000000000000000
_cell_angle_beta 90.000000000000000
_cell_angle_gamma 90.000000000000000
_symmetry_Int_Tables_number 19
_chemical_formula_sum
'C Na '
loop_
_atom_site_label
_atom_site_type_symbol
_atom_site_site_symmetry_multiplicity
_atom_site_occupancy wyckoff
_atom_site_fract_x
_atom_site_fract_y
_atom_site_fract_z
C1 C 4 a 0.4507620388737408 0.2412722355502409 0.2002836109717944
C2 C 4 a 0.7159835056491347 0.7604690269915223 0.1001229603435971
C3 C 4 a 0.7990938581497673 0.7500000000000000 0.0000000000000000
C4 C 4 a 0.5339395625350393 0.2553336754710428 0.3000932659378034
C5 C 4 a 0.7993055002287193 0.7339035928609262 0.4001689503665201
C6 C 4 a 0.4660637764204765 0.7500000000000000 0.0000000000000000
C7 C 4 a 0.7992359572009847 0.7413680362824165 0.7997428117503628
C8 C 4 a 0.5339920062649526 0.2607247608217022 0.8999032511803474
C9 C 4 a 0.4508054785026872 0.2500000000000000 0.9999865914032778
C10 C 4 a 0.7160632668574110 0.7552653191550148 0.6999122605521108
C11 C 4 a 0.4507371346340321 0.2340265058040031 0.5998443164547779
C12 C 4 a 0.7838311343020977 0.2497670407480256 0.0000000000000000
C13 C 4 a 0.4507684383074065 0.2588296507732223 0.7997299759256646
C14 C 4 a 0.7159641189005654 0.7392555506996387 0.8999278505968743
C15 C 4 a 0.5339370177679471 0.2449503259371396 0.6999032756511808
C16 C 4 a 0.7993444489652789 0.7657196483495666 0.5998772927784869
C17 C 4 a 0.7992555146565010 0.7587831215649031 0.2003039368210861
C18 C 4 a 0.5339820054295076 0.2395603206925400 0.1000893926225570
C19 C 4 a 0.7160624746705367 0.7449077831784620 0.3000949858428325
C20 C 4 a 0.4507027849798250 0.2657543547107649 0.4001480943255583
Na1 Na 4 a 0.6252816249467941 0.0000000000000000 0.9281883876001086
Na2 Na 4 a 0.8744455038088575 0.5000000000000000 0.2592461429000107
Na3 Na 4 a 0.8754102156613045 0.9999773581896462 0.7412876496637536
Na4 Na 4 a 0.6245455364933862 0.5000000000000000 0.4102936122942250
Na5 Na 4 a 0.6256409368228546 0.0000000000000000 0.5901517763312539
Na6 Na 4 a 0.8750732446945194 0.5000000000000000 0.5696379329270868
#End

```

Listing 5. CIF file for oS20-NaC₄ containing the VASP optimized lattice constants and atomic positions at 10 GPa.

```

_symmetry_Int_Tables_number 63
_cell_length_a 8.4461896681214643
_cell_length_b 4.9787180730519980
_cell_length_c 4.3158958682925386
_cell_angle_alpha 90.0000000000000000
_cell_angle_beta 90.0000000000000000
_cell_angle_gamma 90.0000000000000000
_symmetry_Int_Tables_number 63
_chemical_formula_sum
'C Na '
loop_
_atom_site_label
_atom_site_type_symbol
_atom_site_site_symmetry_multiplicity
_atom_site_occupancy wyckoff
_atom_site_fract_x
_atom_site_fract_y
_atom_site_fract_z
C1 C 16 h 0.2435236207386140 0.6250134563772747 0.0829306596834911
Na1 Na 4 c 0.0000000000000000 0.2884085523109192 0.2500000000000000
#End

```

Listing 6. CIF file for mP20-NaC₄ containing the VASP optimized lattice constants and atomic positions at 10 GPa.

```

_symmetry_Int_Tables_number 11
_cell_length_a 4.9763713072779092
_cell_length_b 4.2971403813973037
_cell_length_c 8.6995515646003394
_cell_angle_alpha 90.0000000000000000
_cell_angle_beta 99.7172128079009497
_cell_angle_gamma 90.0000000000000000
_symmetry_Int_Tables_number 11
_chemical_formula_sum
'C Na '
loop_
_atom_site_label
_atom_site_type_symbol
_atom_site_site_symmetry_multiplicity
_atom_site_occupancy wyckoff
_atom_site_fract_x
_atom_site_fract_y
_atom_site_fract_z
C1 C 4 f 0.3748660758264677 0.9173775863282644 0.5006096736221578
C2 C 4 f 0.8723223735758482 0.9179787848993116 0.4887063160384884
C3 C 4 f 0.6277710174186169 0.4180513681935950 0.0114755861022431
C4 C 4 f 0.1251066518153792 0.4174037974332522 0.9995767940923272
Na1 Na 2 e 0.4840379642283494 0.2500000000000000 0.7490266449917584
Na2 Na 2 e 0.0180017815718756 0.7500000000000000 0.7504474160489637
#End

```


Listing 7. CIF file for oP18-NaC₈ containing the VASP optimized lattice constants and atomic positions at 10 GPa.

```

_symmetry_Int_Tables_number 51
_cell_length_a 4.2849416211107201
_cell_length_b 7.0408405569361925
_cell_length_c 4.9454256864695196
_cell_angle_alpha 90.0000000000000000
_cell_angle_beta 90.0000000000000000
_cell_angle_gamma 90.0000000000000000
_symmetry_Int_Tables_number 51
_chemical_formula_sum
'C Na '
loop_
_atom_site_label
_atom_site_type_symbol
_atom_site_site_symmetry_multiplicity
_atom_site_occupancy wyckoff
_atom_site_fract_x
_atom_site_fract_y
_atom_site_fract_z
C1 C 8 1 0.5833333333333334 0.8017078173988708 0.1243533376894139
C2 C 8 1 0.9166666666666666 0.7962083500714385 0.6253601678460757
Na1 Na 2 f 0.2500000000000000 0.5000000000000000 0.6984680181220927
#End

```

Listing 8. CIF file for oS44-NaC₁₀ containing the VASP optimized lattice constants and atomic positions at 10 GPa.

```

_symmetry_Int_Tables_number 65
_cell_length_a 4.2701616893271561
_cell_length_b 12.3372454224847932
_cell_length_c 7.0227230974644392
_cell_angle_alpha 90.0000000000000000
_cell_angle_beta 90.0000000000000000
_cell_angle_gamma 90.0000000000000000
_symmetry_Int_Tables_number 65
_chemical_formula_sum
'C Na '
loop_
_atom_site_label
_atom_site_type_symbol
_atom_site_site_symmetry_multiplicity
_atom_site_occupancy wyckoff
_atom_site_fract_x
_atom_site_fract_y
_atom_site_fract_z
C1 C 16 r 0.8333333333333334 0.2998818841363473 0.2986779735933709
C2 C 16 r 0.6660824722040530 0.3998340922640508 0.2940550137969069
C3 C 8 o 0.6672155408982263 0.0000000000000000 0.7077668535232888
Na1 Na 4 i 0.0000000000000000 0.3807971938647299 0.0000000000000000
#End

```

Listing 9. CIF file for hP13-NaC₁₂ containing the VASP optimized lattice constants and atomic positions at 5 GPa.

```
_symmetry_Int_Tables_number 191
_cell_length_a 4.2827286628374583
_cell_length_b 4.2827286628374583
_cell_length_c 7.2725399518830214
_cell_angle_alpha 90.000000000000000
_cell_angle_beta 90.000000000000000
_cell_angle_gamma 120.000000000000142
_symmetry_Int_Tables_number 191
_chemical_formula_sum
'C Na '
loop_
_atom_site_label
_atom_site_type_symbol
_atom_site_site_symmetry_multiplicity
_atom_site_occupancy wyckoff
_atom_site_fract_x
_atom_site_fract_y
_atom_site_fract_z
C1 C 12 n 0.6666666666666666 0.0000000000000000 0.2063351542498993
Na1 Na 1 b 0.0000000000000000 0.0000000000000000 0.5000000000000000
#End
```